biomedicines

Article

Quantitative ECM Profiling Reveals a Recapitulation Gap in a Subcutaneous KPC-Derived Syngeneic PDAC Model

Brahma Mubarak K. Budhwani [1,†], Khidr Kishan K. Budhwani [1,†], Rachael E. Guenter [1,2], Vidhi M. Patel [1], Afrin A. Rupani [1], J. Bart Rose [2] and Karim I. Budhwani [1,3,*]

[1] CerFlux, Birmingham, AL 35203, USA
[2] Department of Surgery, University of Alabama at Birmingham, Birmingham, AL 35203, USA
[3] Hugh Kaul Precision Medicine Institute, University of Alabama at Birmingham, Birmingham, AL 35203, USA
* Correspondence: ironman@cerflux.com
† These authors contributed equally to this work.

Abstract

Background/Objectives: Pancreatic ductal adenocarcinoma (PDAC) develops within a dense desmoplastic stroma that shapes drug transport, mechanotransduction, and therapeutic response. Building on the recapitulation gap framework, we examined whether a commonly used subcutaneous KPC-derived syngeneic model reproduces human PDAC extracellular matrix (ECM) architecture. **Methods:** Dual-stain histochemistry and computational image analysis compared primary human PDAC tumor cores (n = 14 patients) with independently generated syngeneic tumors (n = 3), quantifying collagen and glycosaminoglycan (GAG) signals across compositional, spatial, and textural domains. Inference used one value per patient or animal, and multivariate separation was tested by exact permutation. Local organization was investigated by analyzing 65 simulated cores (sim-cores) from the mouse specimens. **Results:** Mouse tumors showed collagen-dominated architectural divergence, with lower collagen area, approximately seven-fold greater peripheral edge share, and a 2.8-fold lower collagen-to-GAG signal ratio. Human and mouse specimens separated in observed multivariate ECM space (standardized centroid distance 5.18; exact permutation $p = 1/680$); the separation persisted in format-matched sim-cores ($p = 1/680$). Analysis at the two scales identified peripheral collagen organization alongside lower spatial persistence and band fraction. **Conclusions:** Quantitative ECM profiling revealed a recapitulation gap in this model configuration. These findings support feature-specific, fit-for-purpose evaluation when tumor matrix architecture is relevant to the question being studied.

Keywords: pancreatic ductal adenocarcinoma; extracellular matrix; tumor microenvironment; collagen; mouse models; preclinical model fidelity; recapitulation gap

Check for updates

Academic Editor: Bo-Ying Bao

Received: 19 September 2026
Revised: 19 October 2026
Accepted: 20 October 2026
Published: 23 October 2026

Copyright: © 2026 by the authors. Licensee MDPI, Basel, Switzerland. This article is an open access article distributed under the terms and conditions of the Creative Commons Attribution (CC BY) license.

1. Introduction

Pancreatic ductal adenocarcinoma (PDAC) is characterized by a dense, heterogeneous desmoplastic stroma composed of fibrillar collagens, glycosaminoglycans (GAGs), cancer-associated fibroblasts, and other stromal elements. This matrix-rich microenvironment contributes to impaired drug transport, altered immune cell access, and mechanical signaling that can influence tumor cell survival and therapeutic response [1,2]. For these reasons, PDAC stroma has been pursued as a therapeutic target for more than two decades. Yet major stroma-targeting strategies that showed compelling preclinical activity, including

hyaluronan depletion [3,4], Hedgehog pathway inhibition [5,6], and focal adhesion kinase targeting [7,8], have not translated into durable clinical benefit. This persistent pattern of preclinical promise followed by clinical failure has intensified interest in whether the preclinical systems used to evaluate stroma-dependent therapies reproduce the human tumor context in which those therapies must ultimately function.

One underexplored possibility is that preclinical models do not adequately recapitulate the extracellular matrix (ECM) architecture of human PDAC, which is an important component of the tumor context. Fibrillar collagen is a principal structural element of the PDAC stroma, and its abundance and organization contribute to tissue stiffness, interstitial transport, and the physical context experienced by tumor cells [9,10]. Matrix stiffness further engages integrin-mediated mechanosensing, including FAK, Rho/ROCK, and YAP/TAZ signaling, linking ECM architecture to tumor cell proliferation, survival, and invasion [11,12]. Compressive solid stress also accumulates as expanding tumors interact with the surrounding matrix [13]. GAGs, including hyaluronan (HA), contribute an osmotic component to interstitial pressure, but it is the collagen network that provides the structural framework [14,15]. Importantly, these properties do not arise from matrix abundance alone. They emerge from the spatial distribution, compositional balance, texture, and relationships among matrix components [16]. A model may therefore contain the expected stromal constituents while reproducing a substantially different architectural state.

KPC-derived syngeneic models, generated from tumors arising in genetically engineered mice harboring *Kras*^{G12D} and *Trp53*^{R172H} mutations, are workhorses of PDAC drug discovery and development, valued for their immunocompetent context and experimental reproducibility [17–19]. Subcutaneous implantation remains common for efficacy studies because it offers practical advantages for tumor monitoring and response assessment. These strengths, however, do not imply that the model reproduces every feature of human PDAC. Rather, model fidelity is best considered in relation to the biological question being asked. For studies in which intratumoral matrix architecture is expected to influence the endpoint, the relevant issue is whether the model reproduces the ECM features of human disease that are necessary for that application.

This fit-for-purpose view is central to the recently proposed recapitulation gap framework, which describes measurable divergence between patient tumor biology and the corresponding features reproduced by a preclinical model [20]. The framework does not define models as globally valid or invalid; instead, it emphasizes feature-specific benchmarking so that model selection can be matched to the scientific or therapeutic question. This distinction is increasingly relevant as regulatory and scientific priorities shift toward human-relevant preclinical systems and new approach methods (NAMs), while also placing greater emphasis on rigorous characterization of the established models against which newer platforms are compared [21,22]. In this environment, benchmarking established preclinical models becomes essential, not to displace them, but to guide appropriate model selection [19]. Building on this framework, quantitative comparison of ECM architecture provides one way to assess whether a commonly used model configuration reproduces a disease-relevant property of human PDAC. This is particularly consequential for PDAC: if a therapy is designed to act within or through the desmoplastic stroma, the ECM architecture of the preclinical model used to evaluate that therapy is not incidental to the prediction but central to it.

Here, we applied quantitative ECM profiling to primary human PDAC tumors and those from a widely used subcutaneous KPC-derived syngeneic model across compositional, spatial, and textural domains. Using dual-stain histochemistry [23] combined with computational component analysis, we quantified Picrosirius red-positive collagen and

Alcian blue-positive GAG signals as features of tumor matrix architecture. We found a recapitulation gap dominated by collagen-associated signals. The mouse model exhibited reduced intratumoral collagen, pronounced peripheral collagen localization, and altered compositional balance. Whole-section analysis characterized the peripheral phenotype, while format-matched simulated cores (sim-cores) revealed lower spatial persistence, band fraction, and contiguity. The two sampling designs characterize tumor-wide and local components of the architectural divergence. Together, these findings extend the recapitulation gap framework to PDAC and support fit-for-purpose evaluation of preclinical models when tumor matrix architecture is relevant to the question under study.

2. Materials and Methods

2.1. Human Specimens

Primary human PDAC specimens (n = 14) were obtained as a commercial tissue microarray (PA482a; Tissue Array, Derwood, MD, USA). The array comprised 1.5-mm-diameter cores from formalin-fixed, paraffin-embedded (FFPE) resected tumors, sectioned at 5 μm. Pathological diagnosis was independently confirmed by the vendor using H&E and immunohistochemistry. Inclusion criteria required histologically confirmed PDAC and adequate FFPE tissue quality for dual-stain analysis.

Of 48 cores from 24 patients on the array, 28 cores from 14 patients met histological and post-staining quality criteria; six patients were excluded for mounting-medium artifacts. One core per patient was analyzed (n = 14). Patient age ranged from 34 to 68 years (median, 55.5 years); eight were male, and six were female. Stage distribution was IA (n = 1), IIA (n = 7), IIB (n = 3), and IV (n = 3). All selected specimens were surgical resections. The tissue microarray was obtained commercially with appropriate ethical approvals; no additional IRB approval was required for this study.

2.2. Mouse Model

Analyses used archival FFPE blocks of KPC-derived syngeneic tumors generated during a previous, IACUC-approved study; no animals were used specifically for the present work. In the originating study, tumors were established by subcutaneous implantation of KPC-2838c3 cells (7×10^5 cells in 100 μL) into the flank of C57BL/6 mice (The Jackson Laboratory; RRID:IMSR_JAX:000664; 8 weeks old; n = 3). Tumors were harvested 3 weeks after implantation, fixed in formalin, and processed for paraffin embedding. All implanted animals developed tumors and were included in the analysis; no attrition occurred. These archival tumors were generated for a prior study unrelated to matrix characterization, so the ECM architecture analyzed here reflects the model as routinely used rather than tissue prepared to assess the tumor microenvironment.

2.3. Animal Ethics and Procedures

All animal experiments in the originating study that generated the archival FFPE blocks were approved by the IACUC at the University of Alabama at Birmingham (UAB) under Animal Project Number IACUC-22291 (PI: J. Bart Rose; approved 18 December 2024). Methods were performed in accordance with relevant institutional guidelines and national standards for the care and use of laboratory animals. Mice were purchased from The Jackson Laboratory. For procedures requiring anesthesia, mice received 2% isoflurane by inhalation. Euthanasia was performed by primary carbon dioxide (CO_2) inhalation followed by secondary cervical dislocation.

2.4. Histological Staining

Dual chromogenic staining was performed for fibrillar collagen using Picrosirius red and for acidic GAGs using Alcian blue at pH 2.5, as previously described [23]. Although human and mouse slides were prepared by their respective tissue sources, they were both stained using the same reagent lots and dual-stain protocol. Alcian blue at pH 2.5 detects acidic GAG-associated signal and does not distinguish HA from sulfated GAG species. Accordingly, the Alcian blue channel was treated as a GAG-associated signal rather than an HA-specific measurement. Briefly, FFPE sections were deparaffinized in xylene, rehydrated through graded ethanol, and pretreated with 3% acetic acid. Sections were stained sequentially with Alcian blue (20 min), washed in running tap water, then stained with Picrosirius red (60 min). After rinsing in 0.5% acetic acid, the slides were dehydrated and mounted. The complementary blue-red chromogen pair enabled computational spectral separation of Alcian blue-positive and Picrosirius red-positive matrix signals.

2.5. Image Acquisition

Human tissue microarray core specimens and whole-section mouse tumors were imaged using an Agilent BioTek Lionheart FX high-content automated imaging system (Agilent Technologies, Santa Clara, CA, USA; RRID:SCR_019744) at 10× magnification. Images were acquired as RGB stacked TIF files. Human and mouse specimens were imaged using the same acquisition parameters and calibration. Because human specimens were analyzed as tissue microarray cores whereas mouse tumors were analyzed as whole sections, edge-associated measurements were interpreted as configuration-specific spatial descriptors rather than equivalent macroscopic boundary measurements across cohorts.

2.6. Quantitative ECM Profiling

Images were processed using the CerFlux P.E.E.R. imaging and analytics pipeline (Python 3.12.12; NumPy 2.4.1, SciPy 1.17.0, scikit-image 0.26.0), building on the previously described workflow [23]. RGB images were converted to optical density using an incident intensity (I_0) of 255 and computationally unmixed into Picrosirius red-positive and Alcian blue-positive channels. Stain characterization used an optical-density cutoff of 0.15 and red/blue Otsu threshold scales of 0.55 and 1.35, respectively. Tissue detection combined adaptive background-referenced optical-density and brightness criteria with color-based rescue and morphological refinement. A maximum concentration setting of 2.0 controlled concentration-map display rather than capping quantitative values. Both designs used a common image resolution of 1.162 μm per pixel. Each mouse whole section and its derivative sim-cores used the same per-animal parent-section stain calibration, fixing the stain basis and effective thresholds; human cores used per-image stain characterization. ECM architecture is used here operationally to describe two-dimensional stain abundance, distribution, texture, and organization, rather than measured tissue mechanics.

Multivariate profiling used ten hypothesis-guided features spanning matrix composition, localization, texture, and collagen organization: collagen and GAG fractional area, edge share, texture homogeneity, and depth entropy, together with collagen spatial persistence and band fraction. These features represent the primary panel; additional measurements characterize specific aspects of the matrix. Edge share was the fraction of stain-positive area within the outermost 5% of tissue area; depth measures used five boundary-distance shells. Texture was computed after stride-based downsampling to a maximum image dimension of 600 pixels. Collagen contiguity was the area-weighted mean connected-region area ($\Sigma a_i^2/\Sigma a_i$) for 8-connected regions $\geq$ 5 μm^2, reported in units of 10^4 μm^2. Spatial persistence quantified directional agreement between eligible 25 μm tiles separated by approximately 100 μm. Tile directions were derived from

concentration- and coherence-weighted nematic means, and pair agreement was weighted by the product of tile orders. Eligible tiles required at least 5% retained collagen with a defined orientation; images with fewer than 100 contributing pairs were unscored. Persistence ranges from −1 for perpendicular orientations to +1 for parallel orientations, with zero indicating no net nematic agreement. A pixel-pair-weighted implementation was retained as a supporting measure. Collagen-to-GAG ratios used the respective stain-positive areas. Feature definitions, thresholds, and implementation details are provided in Supplementary Table S1.

Nonoverlapping circular sim-cores (1.5 mm diameter) were sampled from the mouse sections to match the human core format. Their circumferences were placed at least 250 µm inside the section so that capsular collagen was not attributed to bulk tumor, mirroring the intent of image-guided biopsy. This margin is an analytical criterion rather than a claim of achievable biopsy precision in murine tumors. MS001, MS002, and MS003 contributed 25, 25, and 15 cores, respectively. Fewer cores fit in smaller tumors; a narrow sectioning tear in MS002 was excluded from anatomical boundary interpretation. Derivative sim-cores retained their parent-section stain calibration. Illustrative orientation maps were selected at the lowest, median, and highest collagen-area ranks within each group among specimens with defined coherence, persistence, and band fraction. Hue encodes orientation and brightness local coherence; maps retain collagen components $\geq 50\ \mu m^2$.

2.7. Statistical Analysis

Between-group inference used one value per independent unit: one core per patient and either one section or the arithmetic mean of available sim-core values per mouse. Averaging preceded $\log_{10}$ transformation of positive ratio and contiguity values for Welch testing and effect-size estimation. Two-sided exact Mann–Whitney tests used untransformed unit values; no ties occurred. Benjamini–Hochberg correction was applied separately within ten primary, eight secondary, and ten supporting measures. Hedges' g is reported as mouse minus human, with model-based 95% intervals for the population standardized difference obtained by noncentral-t inversion under normality and equal-variance assumptions. These intervals are distinct from Welch intervals. With 14 patients and three mice, the minimum two-sided exact Mann–Whitney *p*-value is 2/680. No a priori power calculation was performed for this archival cohort. Descriptive statistics, effect sizes, and univariate comparisons are provided in Supplementary Table S2.

Principal component analysis (PCA) summarized ten hypothesis-guided features after mean centering and scaling to unit variance. PCA visualized individual specimens: 17 images in the whole-section comparison and 69 in the core-format comparison (14 human and 55 mouse cores). Ten additional mouse cores lacked sufficient support for spatial persistence and were excluded from multivariate analysis (Supplementary Table S1); univariate comparisons used available values for each feature. Group separation was tested using centroid distance in the full standardized ten-feature space, after averaging complete-feature specimens within each patient or animal. Exact permutation testing enumerated all 680 assignments of three mouse labels among the 17 independent units. Sensitivity to feature selection was assessed using expanded and correlation-filtered panels; loading stability was assessed by leave-one-patient/animal-out refitting (Supplementary Table S3).

3. Results

3.1. Histological Visualization Reveals Divergent ECM Architecture

Dual-stain histology with computational spectral separation was performed on primary human PDAC tumors (n = 14) and subcutaneous KPC-derived syngeneic mouse tumors (n = 3) (Figure 1). Human tumors showed substantial heterogeneity in ECM architec-

ture, with Picrosirius red-positive collagen distributed throughout the tumor parenchyma to varying degrees (Figure 1A). In contrast, mouse tumors contained markedly less intratumoral collagen, with collagen signal concentrated predominantly at the tumor periphery (Figure 1B).

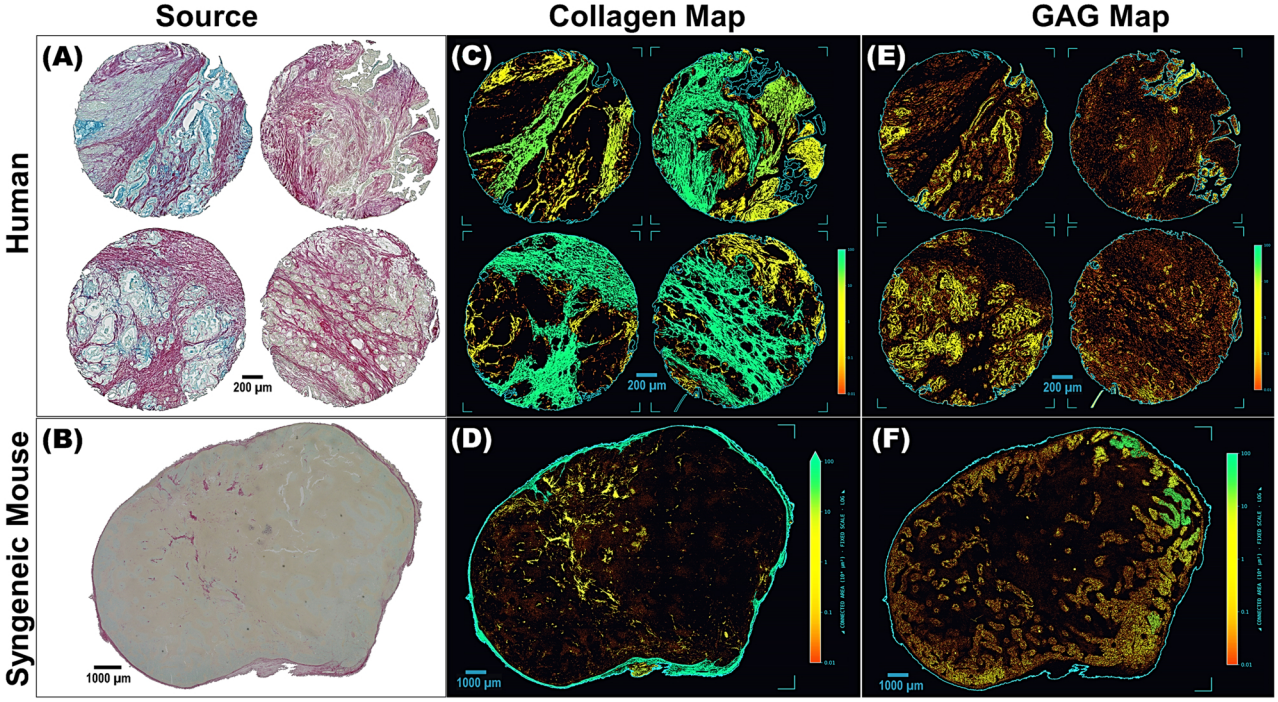


Figure 1. Collagen distribution in human PDAC cores and a subcutaneous mouse tumor section. (**A**) Four representative human cores show variation in matrix abundance and spatial organization. Picrosirius red stains collagen; Alcian blue stains acidic GAG-associated material. (**B**) Mouse section shows sparse interior collagen and conspicuous peripheral staining. (**C**,**D**) Connected-region collagen maps for the human cores and mouse section; (**E**,**F**) corresponding GAG maps. Contiguity maps color each connected region by its area, in units of 10^4 µm^2, on a fixed logarithmic scale of 0.01–100, from rust through gold to green; values outside this range take the endpoint colors. Scale bars: 200 µm (**A**,**C**,**E**) and 1 mm (**B**,**D**,**F**). Human panels show 1.5 mm tissue microarray cores; mouse panels show a whole tumor section, so sampling geometry and scale differ. A format-matched comparison using 1.5 mm sim-cores is presented in Figure 4.

Computational extraction of matrix component maps confirmed these histological differences (Figure 1C–F). Collagen maps from human PDAC showed dense, interwoven signal extending through the tumor cores (Figure 1C), whereas mouse tumors showed sparse intratumoral collagen with pronounced peripheral/capsular localization (Figure 1D). Alcian blue-positive GAG signal was evident in both cohorts (Figure 1E,F). Together, these observations show that principal divergence between cohorts was collagen-associated rather than a uniform reduction in matrix signal.

Within the human cohort, collagen abundance and spatial distribution varied across cores, with matrix organization ranging from diffuse to regionally concentrated. This histological heterogeneity provided the context for quantitative comparison across compositional, spatial, and textural domains.

3.2. Quantitative ECM Profiling Reveals Collagen-Dominated Architectural Divergence

Collagen area was lower in mouse whole sections than in human cores (human 0.325 ± 0.088 vs. mouse 0.134 ± 0.023; g = −2.20, 95% interval −3.78 to −0.80; Welch $q < 0.001$; Mann–Whitney $q = 0.006$; Figure 2A). The collagen-to-GAG ratio was approx-

imately 2.8-fold higher in human specimens (1.64 ± 0.76 vs. 0.58 ± 0.22; g = −1.89, 95% interval −3.39 to −0.53; Welch q = 0.034; Mann–Whitney q = 0.015; Figure 2B).

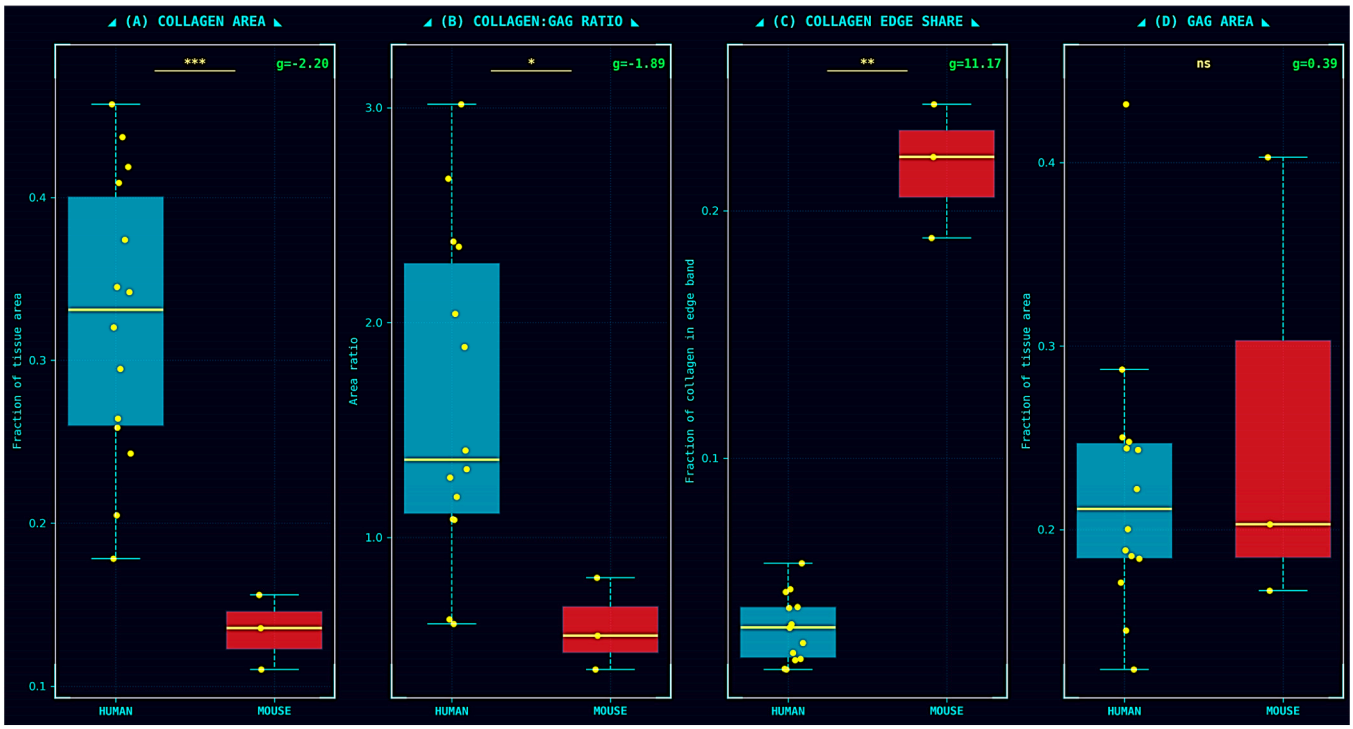


Figure 2. Collagen-associated differences in the whole-section comparison. Boxplots show human cores (n = 14, teal) and mouse sections (n = 3, maroon), with individual specimens overlaid. (**A**) Collagen fractional tissue area. (**B**) Collagen-to-GAG area ratio. (**C**) Collagen edge share, the fraction of collagen within the outermost 5% of tissue area. (**D**) GAG fractional tissue area. Hedges' g (mouse minus human) is −2.20, −1.89, +11.17, and +0.39, respectively; Welch q-values are <0.001, 0.034, 0.013, and 0.768. Values in the text are mean ± SD. Boxes indicate the interquartile range with median lines; whiskers extend to values within 1.5 times the interquartile range. Asterisks denote unadjusted Welch p-values: * $p < 0.05$, ** $p < 0.01$, *** $p < 0.001$; ns, not significant. Inferential conclusions use FDR-adjusted q-values reported in the text and Supplementary Table S2. Edge share in mouse whole sections includes the tumor periphery; the format-matched sim-core comparison is reported in Section 3.4 and Supplementary Table S2.

Collagen edge share showed the largest contrast: 3.2% ± 1.3% in human cores vs. 21.8% ± 2.7% in mouse sections (g = +11.17, 95% interval +7.40 to +16.10; Welch q = 0.013; Mann–Whitney q = 0.006; Figure 2C). This is consistent with the peripheral localization visible in the mouse sections; the format-matched comparison is reported below.

GAG-associated area showed no detected between-group difference (human 0.223 ± 0.075 vs. mouse 0.258 ± 0.127; g = +0.39, 95% interval −0.85 to +1.66; Welch q = 0.768; Figure 2D). The overall pattern was therefore dominated by collagen abundance, localization, and compositional balance. Results for all primary features are in Supplementary Table S2.

3.3. Principal Component Analysis (PCA) Shows Multivariate ECM Space Separation

PCA of the ten-feature panel summarized the major axes of ECM variation (Figure 3). PC1 accounted for 40.7% of the variance and was most strongly associated with collagen edge share (+0.96), collagen depth entropy (−0.96), GAG edge share (−0.79), and collagen area (−0.70). PC2 accounted for 21.2%, with GAG depth entropy as its leading loading (+0.80). PC2 loadings were less stable than PC1 under leave-one-patient/animal-out refitting (Supplementary Table S3).

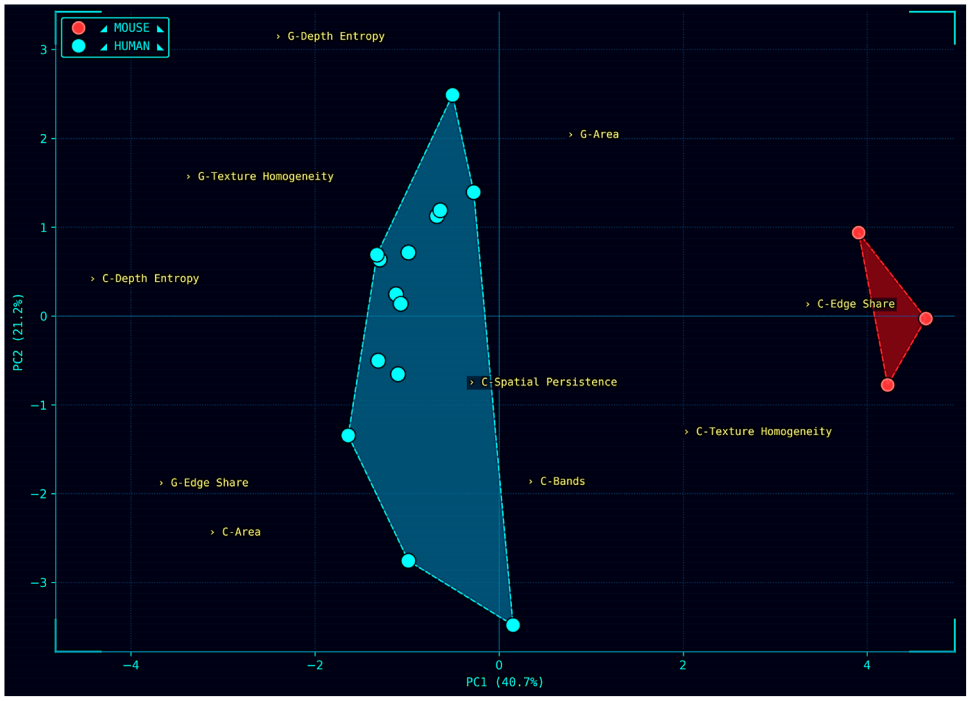


Figure 3. Multivariate ECM separation in the observed cohort. PCA of ten hypothesis-guided features shows 14 human cores and three mouse whole sections. Specimens differ in sampling format: cores versus whole sections. PC1 and PC2 explain 40.7% and 21.2% of variance, respectively. Shaded polygons enclose the observed specimens; they are not confidence regions or population boundaries. The patient/animal-level standardized centroid distance in the full ten-feature space is 5.18 (exact permutation $p = 1/680$). Sensitivity analyses and PCA loading stability are reported in Supplementary Table S3.

Human and mouse specimens separated within the observed multivariate ECM space. Human tumors occupied a broad region predominantly in negative PC1 space, whereas all three mouse tumors occupied positive PC1 space, consistent with their pronounced peripheral collagen organization. The standardized centroid distance between cohorts across the ten hypothesis-guided features was 5.18, exceeding the value for all 679 alternative assignments of mouse labels to three of the 17 specimens (exact permutation $p = 1/680$). Sensitivity to feature selection and PCA loading stability under leave-one-patient/animal-out refitting are summarized in Supplementary Table S3.

3.4. Sim-Cores Reveal Local Collagen Organization Within Mouse Tumors

We next examined 65 interior sim-cores, each 1.5 mm in diameter: 25 from MS001, 25 from MS002, and 15 from MS003. Figure 4A illustrates placement, and Figure 4B–D show collagen-rich regions and corresponding contiguity maps from each animal; selections are collagen-rich regions rather than typical abundance or high-contiguity quantiles. Regional measurements were averaged within each mouse for comparison with the 14 human patients.

Reduced collagen area persisted in the sim-core comparison ($g = -2.88$; both corrected tests $q < 0.01$). Although collagen edge share was higher (5.4% ± 0.6% vs. 3.2% ± 1.3%) in mouse sim-cores than in human cores ($g = +1.71$, 95% interval +0.38 to +3.18; Welch $q = 0.004$; Mann–Whitney $q = 0.029$), it was substantially lower than in mouse whole Sections (21.8% ± 2.7%). The collagen-to-GAG ratio remained lower by Mann–Whitney testing ($q = 0.029$), but not by Welch testing ($q = 0.281$). Collagen depth entropy showed no detected difference (Welch $q = 0.414$; Mann–Whitney $q = 0.172$). GAG texture homogeneity was lower

by both corrected tests, while GAG area showed no detected difference (Supplementary Table S2). Persistence and band fraction are examined in Section 3.5.

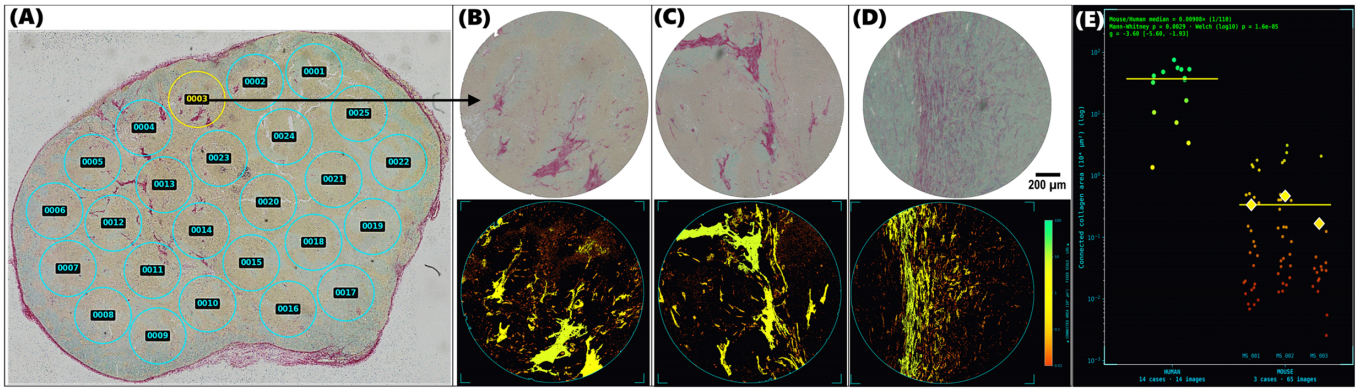


Figure 4. Interior sim-core sampling and collagen contiguity. (**A**) Sim-core placement on mouse MS001, with sim-core circumferences at least 250 µm inside the section margin. (**B**–**D**) Illustrative collagen-rich regions from MS001, MS002, and MS003, respectively, with dual-stained images above and connected-region maps below. Maps show 8-connected collagen regions ≥ 5 µm^2 on a fixed logarithmic scale of 0.01–100 $\times$ 10^4 µm^2, from rust through gold to green. (**E**) Contiguity, $\Sigma a_i^2/\Sigma a_i$, for 14 human cores and 65 mouse sim-cores. Diamonds show independent-unit values: one core value per patient and the mean across sim-cores within each mouse. Horizontal bars show the medians of these independent-unit values within each group. The mouse median is approximately 1/110 of the human median (g = −3.60 on $\log_{10}$ unit values; 95% interval −5.60 to −1.93; exact Mann–Whitney q = 0.015). Inference uses one value per patient or animal, with averaging before transformation. Pixel size is 1.162 µm. Human cores and sim-cores are 1.5 mm in diameter; additional placement criteria are specified in Methods.

Collagen contiguity, measured as area-weighted connected-region area, was markedly lower in mouse sim-cores (Figure 4E). The median of the mouse means was approximately 1/110 of the median across 14 patient values (exact Mann–Whitney $p = 0.0029$, the smallest attainable value; supporting-family; q = 0.015). Welch testing on $\log_{10}$ values was concordant ($p = 1.63 \times 10^{-5}$; q = 8.13×10^{-5}; g = −3.60, 95% interval −5.60 to −1.93). Whole sections showed the reverse direction (g = +1.58; Mann–Whitney q = 0.010; Welch q = 0.079), consistent with large connected peripheral regions. Contiguity therefore captures field-dependent two-dimensional connectivity at these complementary sampling scales.

The ten-feature panel also distinguished human cores from mouse sim-cores at the patient/animal level (centroid distance 4.08; exact permutation $p = 1/680$; Supplementary Table S3).

3.5. Collagen Orientation Maps Reveal Reduced Spatial Persistence and Band Organization

Retained collagen fractional area, measured after excluding components smaller than 50 µm^2, was lower in mouse sim-cores than in human cores (animal means 0.036 ± 0.004 vs. human 0.307 ± 0.086; g = −3.20, 95% interval −5.07 to −1.61; Welch q < 0.001; Mann–Whitney q = 0.015; Figure 5A). Local coherence showed no detected difference after correction by either test in sim-cores (Welch q = 0.083; Mann–Whitney q = 0.243; Figure 5B; Supplementary Table S2).

Spatial persistence at 100 µm was lower in mouse sim-cores (animal means 0.244 ± 0.063 vs. human 0.482 ± 0.146; g = −1.64, 95% interval −3.09 to −0.31; Welch q = 0.005; Mann–Whitney q = 0.041; Figure 5C). Band fraction was also lower (mouse 0.093 ± 0.058 vs. human 0.562 ± 0.156; g = −3.02; both corrected tests q < 0.01; Figure 5D).

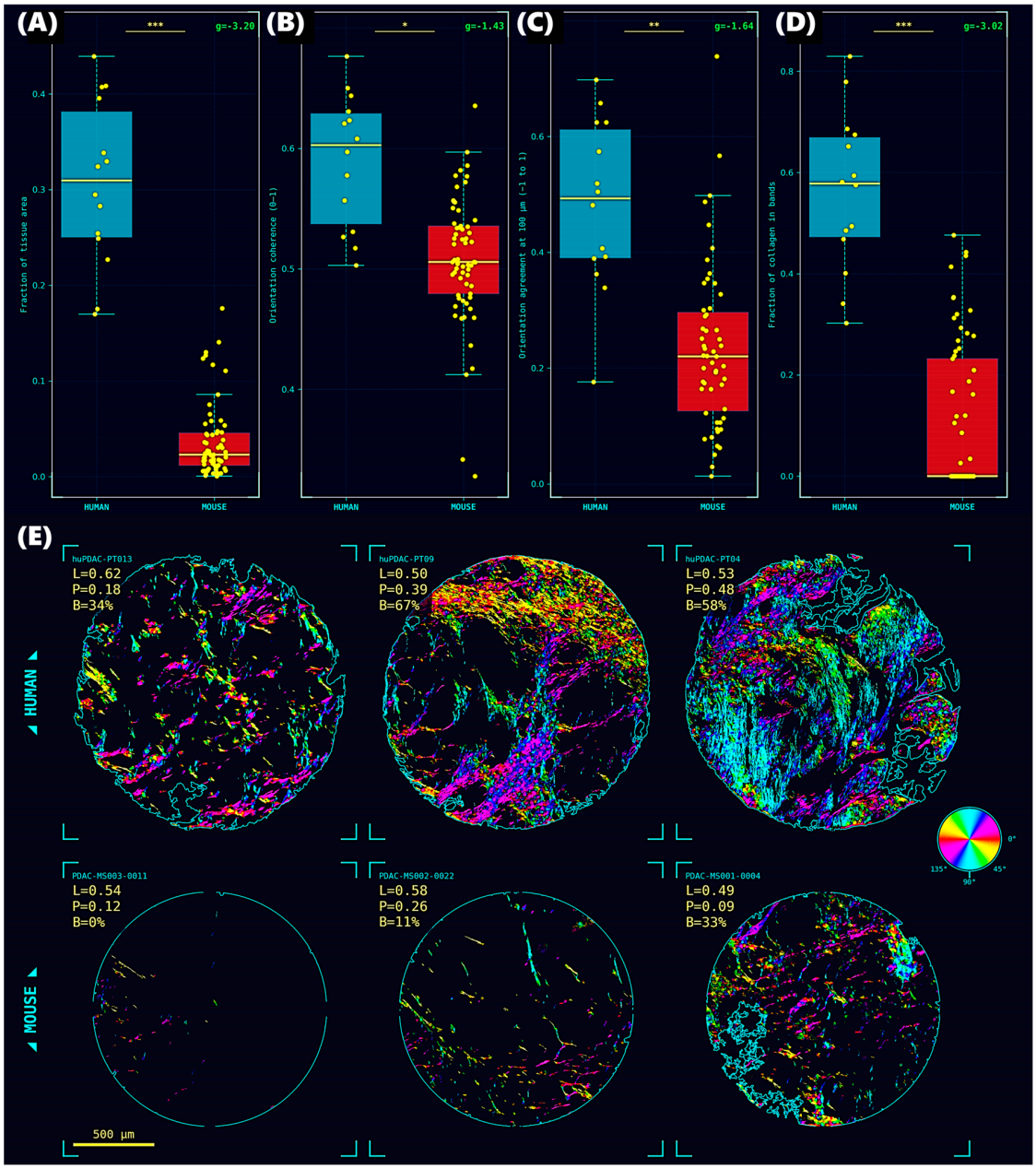


Figure 5. Collagen organization in human cores and mouse sim-cores. (**A**–**D**) Retained collagen fractional area (components $\geq$ 50 µm^2), local coherence, spatial persistence at 100 µm, and band fraction. Points show available individual images: 14 human cores in (**A**–**D**) and 65 mouse sim-cores in (**A**,**B**,**D**); 55 mouse sim-cores have defined spatial persistence in (**C**). Mouse sim-cores derive from three animals. Boxplots summarize image-level distributions; boxes indicate the interquartile range with median lines, and whiskers extend to values within 1.5 times the interquartile range. Hedges' g and unadjusted Welch asterisks use one value per patient or animal, with mouse measurements averaged within animal (14 patients and 3 mice). Hedges' g is −3.20, −1.43, −1.64, and −3.02 for (**A**–**D**), respectively. Asterisks denote unadjusted Welch *p*-values: * $p < 0.05$, ** $p < 0.01$, *** $p < 0.001$; ns, not significant. Inferential conclusions use FDR-adjusted q-values reported in text and Supplementary Table S2; local coherence does not pass correction by either test. (**E**) Six orientation maps show human cores (upper row) and mouse sim-cores (lower row), selected at lowest, median, and highest collagen-area ranks within each group. Mouse examples are MS003-0011, MS002-0022, and MS001-0004 (left to right). Hue encodes direction; brightness encodes local coherence. L, P, and B indicate local coherence, spatial persistence tiled at 100 µm, and collagen band fraction, respectively. Scale bar, 500 µm. Sim-cores are within-animal subsamples, not additional biological replicates.

Orientation maps illustrate local collagen organization underlying these differences (Figure 5E). Human examples show extended collagen structures, whereas mouse examples include sparse regions and collagen-rich tissue with limited directional persistence. Example images were selected by collagen-area rank rather than by organization scores. Among these organization measures, the strongest differences were in spatial persistence and band architecture, supported by both corrected tests.

4. Discussion

Quantitative ECM profiling identified a collagen-dominated recapitulation gap between human PDAC specimens and the subcutaneous KPC-derived syngeneic model examined here. Lower collagen abundance, pronounced peripheral localization, and altered collagen-to-GAG balance accompanied multivariate separation within the observed cohort (Figures 1–3). Sim-cores further characterized the mouse tumor interiors, revealing lower collagen contiguity, spatial persistence, and band fraction. GAG-associated area showed no detected between-group difference, indicating that the divergence was not a uniform reduction in matrix-associated staining. Together, these findings describe a configuration-specific architectural phenotype: a prominent peripheral collagen compartment surrounding an interior with sparse collagen and less extensive organization. The distinction illustrates why model fidelity depends on the distribution and organization of disease-relevant constituents, as well as their presence [20].

Whole-section and sim-core analyses provide complementary views of this phenotype. Whole sections capture the peripheral collagen compartment, including large connected regions that contribute to whole-section contiguity and edge share. Interior sim-cores reveal substantially smaller connected collagen regions and lower persistence and band fraction (Figures 4 and 5). The opposite direction of the contiguity difference at these scales is therefore informative: large peripheral connected regions can coexist with limited interior connectivity (Figure 4). Matching core dimensions provides a common field size, although core circumferences remain artificial boundaries rather than anatomical tumor margins. Core edge share and depth entropy consequently describe organization relative to the sampled field. A core-only analysis would omit the tumor-wide peripheral arrangement, whereas a whole-section summary would obscure differences in interior organization. Considering both scales reveals how collagen is distributed between compartments and organized within them.

Human PDAC studies describe heterogeneous collagen organization around and between malignant glands, including differences in fiber alignment, length, and width relative to nonmalignant pancreatic tissue [24,25]. These observations provide a biological context for examining collagen organization beyond abundance. Our measurements distinguish several aspects of that organization: persistence over approximately 100 μm and band fraction were lower in mouse interiors after multiplicity correction, whereas local coherence showed no detected difference after correction (Figure 5). These brightfield-derived measures describe the spatial extent and arrangement of collagen-associated signal and are not interchangeable with fiber-level measurements obtained by second harmonic generation or polarization microscopy. Published alignment measurements likewise address a distinct endpoint; one study detected no significant alignment difference between human tumor-core and infiltrating-edge regions [26]. Taken together, the present observations suggest that the principal organizational differences concern the extent and arrangement of collagen structures across space, rather than a uniform reduction in local directional order.

The component specificity of the findings is also important. Collagen-associated features differed across several measured domains, whereas GAG-associated area showed no detected difference. This does not establish equivalent GAG abundance or organization:

uncertainty remains substantial, and GAG texture homogeneity differed in the sim-core comparison (Supplementary Table S2). Alcian blue at pH 2.5 detects acidic GAG-associated material without distinguishing HA from sulfated GAG species. Similar stained area therefore cannot establish preservation of HA abundance or biological activity. The collagen-to-GAG ratio describes the balance of the two measured chromogenic signals rather than the molecular composition of the GAG compartment. The resulting picture is one of selective divergence across matrix features, emphasizing the importance of evaluating individual components within their broader spatial context.

For therapies intended to penetrate, remodel, or act within desmoplastic tissue, matrix architecture is part of the experimental condition. Collagen abundance, crosslinking, and organization can influence the mechanical environment experienced by tumor and stromal cells [9,27], while matrix mechanics and solid stress can affect signaling and transport [13,28]. A collagen-sparse interior surrounded by a prominent peripheral compartment presents a different spatial context from collagen distributed throughout sampled tumor tissue. Its functional significance may depend on where therapy enters, which compartment it targets, and whether its activity requires matrix penetration or remodeling. Potential downstream effects include altered integrin-associated signaling, FAK and YAP/TAZ activity, and stiffness-responsive miRNA and lncRNA programs [11,12,29]. These endpoints were not measured here, and two-dimensional stain connectivity and directional persistence are not direct measurements of mechanics or transport. The phenotype nevertheless gives functional studies specific structural features to investigate: interior contiguity, directional persistence, band organization, and peripheral collagen concentration.

Several features of the study define its scope. Fourteen human patients and three archival mouse tumors provide evidence of divergence within this cohort but limited precision for broader population estimates. Sim-cores improve regional characterization without increasing biological replication; inference therefore used one value per patient or animal. Exact permutation analysis assesses separation under its exchangeability assumptions rather than performance in independent specimens. Human and mouse tissues differed in provenance and preparation, leaving potential fixation and other preanalytical effects despite shared staining reagents, protocols, and acquisition conditions. Specimen acquisition and adequacy are additional considerations when extending ECM profiling to pancreatic biopsy material, as highlighted by studies of endoscopic ultrasound-guided tissue sampling [30,31]. Human cores provide limited anatomical coverage, with their positions relative to the tumor margin unspecified, whereas mouse sim-cores sample defined interior regions. Human stain calibration was performed per image, while mouse derivatives retained their parent-section calibration. Multivariate analysis further represents the subset of mouse cores with sufficient collagen support for persistence measurement and may underrepresent the sparsest regions. All measurements remain conditional on segmentation and two-dimensional sectioning. Finally, implantation site, KPC-derived cell-line characteristics, syngeneic host context, and tumor growth history cannot be disentangled in this design. Same-cell comparisons across subcutaneous and orthotopic settings would help assess site-associated effects, with additional lines and hosts addressing other sources of variation. Archival tissue use avoided generating additional animals, and the resulting observations provide a defined configuration for these subsequent comparisons.

The practical implication is that matrix context should be measured when it is relevant to the experimental endpoint. This study identifies specific ECM differences in one subcutaneous model configuration without assigning suitability across all applications or establishing the superiority of another platform. For studies centered on collagen remodeling, stromal transport, or mechanotransduction, comparable characterization across orthotopic tumors, patient-derived systems, ex vivo tissue, and engineered models could

help determine which platform reproduces the required features [19,32]. The increasing emphasis on human-relevant models and new approach methodologies reinforces the value of such empirical benchmarking [21,22]. Independent cohorts, anatomically matched sampling, complementary matrix imaging, and coupled functional measurements offer a path from architectural comparison to endpoint-specific model evaluation. Quantitative ECM profiling provides an empirical basis for choosing models according to the matrix features that a scientific question requires.

5. Conclusions

Quantitative ECM profiling identified a collagen-dominated recapitulation gap between human PDAC specimens and the subcutaneous KPC-derived syngeneic model examined here. Complementary whole-section and sim-core analyses distinguished peripheral collagen accumulation from reduced interior collagen abundance and organization, demonstrating why the presence of stromal components alone cannot establish architectural fidelity. These findings characterize the observed cohort and support feature-specific, fit-for-purpose benchmarking across preclinical platforms. For PDAC studies in which matrix context is relevant, quantitative ECM profiling provides an empirical basis for model comparison and selection. Fit-for-purpose model selection should be grounded in measured correspondence to the human disease features required by the experimental question.

Supplementary Materials: The following supporting information can be downloaded at: https://www.mdpi.com/article/10.3390/biomedicines14112421/s1, Table S1, ECM feature definitions, analytical settings, and sampling information; Table S2, patient/animal-level univariate ECM comparisons; Table S3, multivariate sensitivity analyses, PCA loading stability, and primary-feature loadings.

Author Contributions: B.M.K.B. and K.K.K.B. are co-first authors. Conceptualization, K.I.B.; data curation, R.E.G., K.K.K.B., B.M.K.B., V.M.P., and K.I.B.; formal analysis, R.E.G., K.K.K.B., B.M.K.B., and K.I.B.; funding acquisition, K.I.B.; investigation, R.E.G., K.K.K.B., B.M.K.B., V.M.P., and A.A.R.; methodology, K.K.K.B., B.M.K.B., R.E.G., and K.I.B.; project administration, K.I.B.; resources, R.E.G. and K.I.B.; supervision, R.E.G. and K.I.B.; validation, J.B.R.; writing—original draft preparation, K.K.K.B., B.M.K.B., R.E.G., V.M.P., and K.I.B.; writing—review and editing, All authors. All authors have read and agreed to the published version of the manuscript.

Funding: This work was funded by CerFlux, Innovate Alabama, the National Science Foundation, grants TI-2321805 and TI-2545371 (KIB), and the National Cancer Institute at the National Institutes of Health, grant 1R43CA254493-01 (KIB).

Institutional Review Board Statement: Human specimens were commercially obtained, de-identified archival tissues and did not require additional institutional review board approval. Animal tissues analyzed in this study were archival specimens generated under a previously approved University of Alabama at Birmingham IACUC protocol (APN IACUC-22291), approval date 18 December 2024.

Informed Consent Statement: Not applicable.

Data Availability Statement: Supporting data are available from the corresponding author on an individual basis, subject to applicable permissions and agreements. Available materials can include specimen-level feature values, core-to-animal mappings, animal-level summaries, effective parameters, calibration records, detailed metric definitions, and source or representative images where permitted. Licensing and intellectual-property considerations do not permit public deposition of the proprietary software implementation.

Acknowledgments: We thank our colleagues at the Hugh Kaul Precision Medicine Institute at UAB, the O'Neal Comprehensive Cancer Center, the Alabama School of Fine Arts, and the Aga Khan University Nairobi Cancer Center for their support and collaboration. Generative AI tools from OpenAI and Anthropic were used for journal-specific framing, critical review of manuscript text,

critical review of computational code (including assistance with regression and unit testing), and formatting Supplementary Tables. All reported image processing, statistical calculations, table values, and figure generation were performed by deterministic computational algorithms. Generative AI was not used to synthesize experimental images or specimen-level measurements. The authors reviewed and verified the output and take full responsibility for the content of the published article.

Conflicts of Interest: Dr. Budhwani is co-founder and CEO-Scientist of CerFlux and a co-inventor on issued and pending patents relating to human-relevant cancer model platforms, including in vitro, ex vivo, in silico, and cancer supermodel technologies. He serves on scientific and advisory boards for the Breast Cancer Research Foundation of Alabama, the American Cancer Society of Alabama, BIO Alabama, Coe College, and the Department of Biomedical Engineering at the University of Alabama at Birmingham.

Abbreviations

The following abbreviations are used in this manuscript:

ECM	Extracellular matrix
FAK	Focal adhesion kinase
FDA	U.S. Food and Drug Administration
FFPE	Formalin-fixed, paraffin-embedded
GAGs	Glycosaminoglycans
GLCM	Gray-level co-occurrence matrix
HA	Hyaluronan
IACUC	Institutional Animal Care and Use Committee
IRB	Institutional review board
NAMs	New Approach Methods; New Approach Methodologies; Novel Alternative Methods
PCA	Principal component analysis
PDAC	Pancreatic ductal adenocarcinoma
ROCK	Rho-associated coiled-coil-containing protein kinase
ROI	Region of interest
TMA	Tissue microarray
TME	Tumor microenvironment
YAP/TAZ	Yes-associated protein/transcriptional coactivator with PDZ-binding motif

References

1. Erkan, M.; Hausmann, S.; Michalski, C.W.; Fingerle, A.A.; Dobritz, M.; Kleeff, J.; Friess, H. The Role of Stroma in Pancreatic Cancer: Diagnostic and Therapeutic Implications. *Nat. Rev. Gastroenterol. Hepatol.* **2012**, *9*, 454–467. [CrossRef]
2. Prakash, J.; Shaked, Y. The Interplay between Extracellular Matrix Remodeling and Cancer Therapeutics. *Cancer Discov.* **2024**, *14*, 1375–1388. [CrossRef]
3. Hingorani, S.R.; Zheng, L.; Bullock, A.J.; Seery, T.E.; Harris, W.P.; Sigal, D.S.; Braiteh, F.; Ritch, P.S.; Zalupski, M.M.; Bahary, N.; et al. HALO 202: Randomized Phase II Study of PEGPH20 Plus Nab-Paclitaxel/Gemcitabine Versus Nab-Paclitaxel/Gemcitabine in Patients With Untreated, Metastatic Pancreatic Ductal Adenocarcinoma. *J. Clin. Oncol.* **2018**, *36*, 359–366. [CrossRef]
4. Van Cutsem, E.; Tempero, M.A.; Sigal, D.; Oh, D.Y.; Fazio, N.; MacArulla, T.; Hitre, E.; Hammel, P.; Hendifar, A.E.; Bates, S.E.; et al. Randomized Phase III Trial of Pegvorhyaluronidase Alfa with Nab-Paclitaxel plus Gemcitabine for Patients with Hyaluronan-High Metastatic Pancreatic Adenocarcinoma. *J. Clin. Oncol.* **2020**, *38*, 3185–3194. [CrossRef]
5. Olive, K.P.; Jacobetz, M.A.; Davidson, C.J.; Gopinathan, A.; McIntyre, D.; Honess, D.; Madhu, B.; Goldgraben, M.A.; Caldwell, M.E.; Allard, D.; et al. Inhibition of Hedgehog Signaling Enhances Delivery of Chemotherapy in a Mouse Model of Pancreatic Cancer. *Science* **2009**, *324*, 1457–1461. [CrossRef]
6. Rhim, A.D.; Oberstein, P.E.; Thomas, D.H.; Mirek, E.T.; Palermo, C.F.; Sastra, S.A.; Dekleva, E.N.; Saunders, T.; Becerra, C.P.; Tattersall, I.W.; et al. Stromal Elements Act to Restrain, Rather than Support, Pancreatic Ductal Adenocarcinoma. *Cancer Cell* **2014**, *25*, 735–747. [CrossRef]
7. Jiang, H.; Hegde, S.; Knolhoff, B.L.; Zhu, Y.; Herndon, J.M.; Meyer, M.A.; Nywening, T.M.; Hawkins, W.G.; Shapiro, I.M.; Weaver, D.T.; et al. Targeting Focal Adhesion Kinase Renders Pancreatic Cancers Responsive to Checkpoint Immunotherapy. *Nat. Med.* **2016**, *22*, 851–860. [CrossRef]

8. Wang-Gillam, A.; Lim, K.H.; McWilliams, R.; Suresh, R.; Lockhart, A.C.; Brown, A.; Breden, M.; Belle, J.I.; Herndon, J.; Bogner, S.J.; et al. Defactinib, Pembrolizumab, and Gemcitabine in Patients with Advanced Treatment Refractory Pancreatic Cancer: A Phase I Dose Escalation and Expansion Study. *Clin. Cancer Res.* **2022**, *28*, 5254–5262. Erratum in *Clin. Cancer Res.* **2022**, *29*, 4698. https://doi.org/10.1158/1078-0432.CCR-23-2993. [CrossRef]
9. Nia, H.T.; Munn, L.L.; Jain, R.K. Physical Traits of Cancer. *Science* **2020**, *370*, eaaz0868. [CrossRef]
10. Jain, R.K.; Martin, J.D.; Stylianopoulos, T. The Role of Mechanical Forces in Tumor Growth and Therapy. *Annu. Rev. Biomed. Eng.* **2014**, *16*, 321–346. [CrossRef]
11. Paszek, M.J.; Zahir, N.; Johnson, K.R.; Lakins, J.N.; Rozenberg, G.I.; Gefen, A.; Reinhart-King, C.A.; Margulies, S.S.; Dembo, M.; Boettiger, D.; et al. Tensional Homeostasis and the Malignant Phenotype. *Cancer Cell* **2005**, *8*, 241–254. [CrossRef]
12. Dupont, S.; Morsut, L.; Aragona, M.; Enzo, E.; Giulitti, S.; Cordenonsi, M.; Zanconato, F.; Le Digabel, J.; Forcato, M.; Bicciato, S.; et al. Role of YAP/TAZ in Mechanotransduction. *Nature* **2011**, *474*, 179–184. [CrossRef]
13. Stylianopoulos, T.; Martin, J.D.; Chauhan, V.P.; Jain, S.R.; Diop-Frimpong, B.; Bardeesy, N.; Smith, B.L.; Ferrone, C.R.; Hornicek, F.J.; Boucher, Y.; et al. Causes, Consequences, and Remedies for Growth-Induced Solid Stress in Murine and Human Tumors. *Proc. Natl. Acad. Sci. USA* **2012**, *109*, 15101–15108. [CrossRef]
14. Provenzano, P.P.; Hingorani, S.R. Hyaluronan, Fluid Pressure, and Stromal Resistance in Pancreas Cancer. *Br. J. Cancer* **2013**, *108*, 1–8. [CrossRef]
15. Dufort, C.C.; DelGiorno, K.E.; Carlson, M.A.; Osgood, R.J.; Zhao, C.; Huang, Z.; Thompson, C.B.; Connor, R.J.; Thanos, C.D.; Scott Brockenbrough, J.; et al. Interstitial Pressure in Pancreatic Ductal Adenocarcinoma Is Dominated by a Gel-Fluid Phase. *Biophys. J.* **2016**, *110*, 2106–2119. [CrossRef]
16. Velez, D.O.; Ranamukhaarachchi, S.K.; Kumar, A.; Modi, R.N.; Lim, E.W.; Engler, A.J.; Metallo, C.M.; Fraley, S.I. 3D Collagen Architecture Regulates Cell Adhesion through Degradability, Thereby Controlling Metabolic and Oxidative Stress. *Integr. Biol.* **2019**, *11*, 221–234. [CrossRef]
17. Hingorani, S.R.; Petricoin, E.F.; Maitra, A.; Rajapakse, V.; King, C.; Jacobetz, M.A.; Ross, S.; Conrads, T.P.; Veenstra, T.D.; Hitt, B.A.; et al. Preinvasive and Invasive Ductal Pancreatic Cancer and Its Early Detection in the Mouse. *Cancer Cell* **2003**, *4*, 437–450. [CrossRef]
18. Hingorani, S.R.; Wang, L.; Multani, A.S.; Combs, C.; Deramaudt, T.B.; Hruban, R.H.; Rustgi, A.K.; Chang, S.; Tuveson, D.A. Trp53R172H and KrasG12D Cooperate to Promote Chromosomal Instability and Widely Metastatic Pancreatic Ductal Adenocarcinoma in Mice. *Cancer Cell* **2005**, *7*, 469–483. [CrossRef]
19. Budhwani, K.I.; Patel, Z.H.; Guenter, R.E.; Charania, A.A. A Hitchhiker's Guide to Cancer Models. *Trends Biotechnol.* **2022**, *40*, 1361–1373. [CrossRef]
20. Budhwani, K.I.; Stringer-Reasor, E.M.; Sorace, A.G.; Buchsbaum, D.J.; Crawford, C.L. Closing the Recapitulation Gap in Obesity-Conditioned TNBC Drug Development. *npj Drug Discov.* **2026**, *3*, 39. [CrossRef]
21. U.S. Food and Drug Administration (FDA). General Considerations for the Use of New Approach Methodologies in Drug Development: Draft Guidance for Industry. Center for Drug Evaluation and Research: Silver Spring, MD, USA,, 2026. Available online: https://www.fda.gov/media/191589/download (accessed on 18 September 2026).
22. National Institutes of Health. Selecting the Right Models for Your Research: A Focus on New Approach Methodologies (NAMs). Available online: https://grants.nih.gov/news-events/nih-extramural-nexus-news/2026/05/selecting-the-right-models-for-your-research-a-focus-on-new-approach-methodologies-nams (accessed on 19 September 2026).
23. Boykin, L.A.; Jayashankar, S.; Budhwani, K.K.K.; Budhwani, B.M.K.; Samal, D.; Crawford, C.L.; Tsung, A.; Budhwani, K.I. Protocol for Spatial Characterization of ECM Collagen-GAG in Colorectal Cancer Tumor Microenvironment. *bioRxiv* **2025**, 1–15. [CrossRef]
24. Drifka, C.R.; Tod, J.; Loeffler, A.G.; Liu, Y.; Thomas, G.J.; Eliceiri, K.W.; Kao, W.J. Periductal Stromal Collagen Topology of Pancreatic Ductal Adenocarcinoma Differs from That of Normal and Chronic Pancreatitis. *Mod. Pathol.* **2015**, *28*, 1470–1480. [CrossRef]
25. Chitsaz, M.; Yang, L.; Rayes-Danan, R.; Savari, O.; Li, B.; Shribak, M.; Eliceiri, K.; Loeffler, A. Polychromatic Polarization Microscopy Differentiates Collagen Fiber Signatures in Benign Pancreatic Tissue and Pancreatic Ductal Adenocarcinoma. *Mod. Pathol.* **2025**, *38*, 100768. [CrossRef]
26. Drifka, C.R.; Loeffler, A.G.; Mathewson, K.; Keikhosravi, A.; Eickhoff, J.C.; Liu, Y.; Weber, S.M.; John Kao, W.; Eliceiri, K.W. Highly Aligned Stromal Collagen Is a Negative Prognostic Factor Following Pancreatic Ductal Adenocarcinoma Resection. *Oncotarget* **2016**, *7*, 76197–76213. [CrossRef]
27. Levental, K.R.; Yu, H.; Kass, L.; Lakins, J.N.; Egeblad, M.; Erler, J.T.; Fong, S.F.T.; Csiszar, K.; Giaccia, A.; Weninger, W.; et al. Matrix Crosslinking Forces Tumor Progression by Enhancing Integrin Signaling. *Cell* **2009**, *139*, 891–906. [CrossRef]
28. Chaudhuri, O.; Cooper-White, J.; Janmey, P.A.; Mooney, D.J.; Shenoy, V.B. Effects of Extracellular Matrix Viscoelasticity on Cellular Behaviour. *Nature* **2020**, *584*, 535–546. [CrossRef]

29. Campos-Parra, A.D.; Puente-Rivera, J.; López-Camarillo, C.; Nuñez-Olvera, S.I.; Hernández Nava, N.; Macias, G.A.; Silva-Cázares, M.B. The Stiff Side of Cancer: How Matrix Mechanics Rewrites Non-Coding RNA Expression Programs. *Non-Coding RNA* **2026**, *12*, 7. [CrossRef]
30. Facciorusso, A.; Stasi, E.; Di Maso, M.; Serviddio, G.; Ali Hussein, M.S.; Muscatiello, N. Endoscopic Ultrasound-Guided Fine Needle Aspiration of Pancreatic Lesions with 22 versus 25 Gauge Needles: A Meta-Analysis. *United Eur. Gastroenterol. J.* **2017**, *5*, 846–853. [CrossRef]
31. Mangiavillano, B.; Crinò, S.F.; Facciorusso, A.; Di Matteo, F.; Barbera, C.; Larghi, A.; Rizzatti, G.; Carrara, S.; Spadaccini, M.; Auriemma, F.; et al. Endoscopic Ultrasound-Guided Fine-Needle Biopsy with or without Macroscopic on-Site Evaluation: A Randomized Controlled Noninferiority Trial. *Endoscopy* **2023**, *55*, 129–137. [CrossRef]
32. Tomás-Bort, E.; Kieler, M.; Sharma, S.; Candido, J.B.; Loessner, D. 3D Approaches to Model the Tumor Microenvironment of Pancreatic Cancer. *Theranostics* **2020**, *10*, 5074–5089. [CrossRef]

Disclaimer/Publisher's Note: The statements, opinions and data contained in all publications are solely those of the individual author(s) and contributor(s) and not of MDPI and/or the editor(s). MDPI and/or the editor(s) disclaim responsibility for any injury to people or property resulting from any ideas, methods, instructions or products referred to in the content.